THE JOURNAL OF PHYSICAL CHEMISTRY C

ARTICLE

pubs.acs.org/JPCC

Modeling ZnS and ZnO Nanostructures: Structural, Electronic, and Optical Properties

Jon M. Azpiroz,[†,‡] Edoardo Mosconi,[‡] and Filippo De Angelis*[,‡]

[†]Kimika Fakultatea, Euskal Herriko Unibertsitatea and Donostia International Physics Center (DIPC), P.K. 1072 Donostia, Euskadi, Spain

[‡]Istituto CNR di Scienze e Tecnologie Molecolari (ISTM-CNR), c/o Dipartimento di Chimica, Università di Perugia, Via elce di Sotto 8, I-06213, Perugia, Italy

Supporting Information

ABSTRACT: We report the computational modeling of ZnS and ZnO nanostructures by defining realistic nanoparticle models ~1.5 nm sized for each material and investigating their structural, electronic, and optical properties by means of DFT/TDDFT calculations. To provide a direct comparison of calculated data to experimentally characterized nanoparticles, 3D $(ZnX)_{111}$ nanoclusters of prismatic shape have been set up starting from the bulk wurtzite (X = O, S), with two different saturation patterns of the polar surfaces. The investigated models have been optimized by means of Car−Parrinello molecular dynamics and local geometry optimization techniques. The investigated systems exhibit a well-opened HOMO−LUMO energy gap, without any artificial intraband-gap states. TDDFT calculation of the lowest excitation energies are in excellent agreement, within 0.1−0.2 eV, with the experimental absorption onsets reported for similarly sized ZnO and ZnS nanoparticles (3.70 and 4.40 eV, respectively). We have also investigated the electronic structure of the considered nanoparticles, with reference to the valence band structure, finding calculated binding energies for the Zn d-shell to be only slightly displaced toward lower values compared to experimental values, possibly due to quantum confinement effects. This work provides the required computational framework for modeling ZnX and in general II−VI semiconductor nanomaterials, opening the way to simulation of ligand/semiconductor interactions.

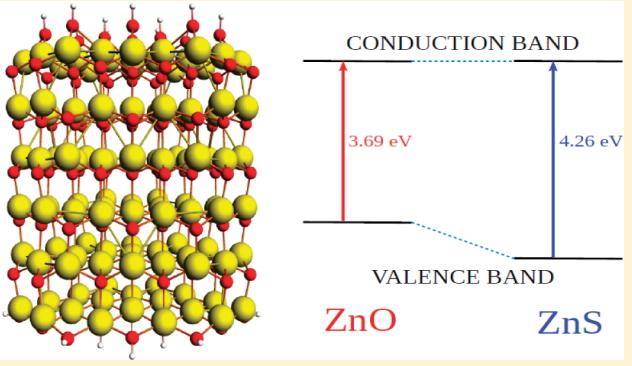

1. INTRODUCTION

II−VI semiconductor nanomaterials have been deeply investigated due to their unique photophysical properties, which substantially deviate from those of their bulk counterparts.[1] At the nanoscale, charge carriers are confined to move within regions of the space comparable to their de Broglie wavelength. Such quantum confinement results in a discrete size- and shape-dependent structure of electronic levels and in the appearance of fascinating properties. Promising technological applications of II−VI semiconductor nanomaterials such as photooxidizers and photocatalists,[2,3] photovoltaic solar cells,[4−7] quantum devices,[8] optical sensitizers,[9] and fluorescent probes[10] have been developed due to their wide absorption range, size-tunable emission, high luminescence efficiency, unmatched photostability, and reasonably long photoexcited lifetimes.[1]

ZnO and ZnS are among the most studied II−VI compounds. Their wide direct band gaps (3.4 and 3.7 eV respectively) and high exciton binding energies (60 and 40 meV respectively) make ZnO and ZnS particularly suitable for optoelectronic applications.[11] Besides, they are abundant, highly stable, and environmentally friendly materials so that they are amenable also for biomedical applications. Both ZnO and ZnS can adopt three phases, namely, cubic sphalerite (B3 phase in the *Strukturbericht* notation), hexagonal wurtzite (B4), or the rarely observed cubic rock salt (B1). Wurtzite is the most stable polymorph of ZnO at room temperature. On the contrary, ZnS crystallizes in sphalerite under ambient conditions, while wurtzite polymorph is stable above 1020 °C. Nevertheless, with decreasing particle size, the surface-to-volume ratio becomes large enough so that the stability of the two phases is influenced by the surface energy. It has been suggested theoretically that the mean surface energy of a three-dimensional nanoparticle is greater for the sphalerite than for wurtzite.[12−14] This prediction has found support in recent experimental works reporting the low-temperature synthesis of small wurtzite ZnS nanoparticles.[15−20] Interestingly, the hexagonal wurtzite polymorph exhibits better luminescent properties than the cubic sphalerite phase.[21] It is worth noting, however, that the surface energy and therefore the crystal structure of the

Received: August 30, 2011
Revised: November 15, 2011
Published: November 16, 2011

dx.doi.org/10.1021/jp2083709 | *J. Phys. Chem. C* 2011, 115, 25219–25226

nanoparticle strongly depend on the synthesis conditions. A wide range of ZnO and ZnS nanostructures have been obtained by choosing the appropriate temperature, solvent, or coordinating ligands.[11] Moreover, postsynthesis reversible structural transformations at room temperature have been observed by absorption−desorption of methanol and water on the surface of ZnS nanoparticles.[22]

Particularly interesting is the size- and shape-dependency of the optical properties of the ZnS and ZnO nanostructures. Due to the quantum confinement mentioned before, a blue-shift of both the absorption and emission spectral onsets is observed with decreasing structural size. The absorption onsets of 0.7−1.5 nm radii ZnO particles appear in the range 3.7−3.8 eV, which are found to red-shift toward the bulk band-gap value of 3.3−3.4 eV upon increasing the particle size.[23−25] The ZnO visible light emission usually falls in the green−yellow region of the spectrum (2.1−2.4 eV), even if blue (2.7−2.8 eV) and orange (1.8−1.9 eV) emissions have also been reported.[23−26] Most of the literature suggests that the green luminescence of ZnO arises from oxygen vacancies, with long-lived visible emission (∼microsecond range) consistently reported along with a short-lived (∼nanosecond range) blue luminescence.[23−25] A size-dependent shift of the visible luminescence was also reported.[23−25]

ZnS wurtzite nanoparticles of 0.75−2.00 nm radii show absorption onsets in the range 3.9−4.4 eV,[20,27,28] which are blue-shifted with respect to the bulk band gap of 3.7 eV. With the increasing size of the nanoparticle, the absorption is found to converge toward the bulk value. For particles whose radius is greater than the exciton radius of bulk ZnS (2.5 nm), no quantum confinement effect is observed in the absorption.[18,19,29] The visible light emission of ZnS has been widely reported in the literature. As in the case of ZnO, the origin of such luminescence remains a debated issue. Kar et al. reported three emission peaks at ∼3.1, 2.8, and 2.5 eV for wurtzite ZnS nanowires and nanoribbons.[30−32] The first one was suggested to arise from sulfur vacancies and interstitial lattice defects, and the second and the third one were attributed to surface states and zinc vacancies, respectively. Since wurtzite ZnS nanoparticles show similar emission features, their luminescence properties have been explained in the same framework.[27] Tang et al. distinguished three peaks at 3.2, 3.1 and 3.0 eV in the emission spectrum of ∼3 nm sized sphalerite ZnS nanoparticles.[33] The emission peaks at 3.1 and 3.0 eV were ascribed to surface states and internal vacancies, respectively. The peak at 3.22 eV may be related to the dangling bonds of the surface-attached ligands.

Along with the remarkable amount of experimental investigations, theoretical calculations have contributed to shed light on the structural and electronic properties of ZnO and ZnS. Several works focused on the structural and defective properties of ZnO.[34−40] Most of them addressed the bulk material, and only a few investigations were performed on nanostructure models.[41−45] Due to computational limitations, early theoretical studies of ZnS nanostructures focused on small clusters and on their structural characterization. Global minimization techniques predict that $(ZnS)_n$ clusters with $n \sim 10-50$ adopt hollow spherical structures, where all atoms are three-coordinated.[46−49] Similar studies by Hamad et al. regarding particles with sizes in the range $n \sim 50-80$ produced core−shell structures in which one spherical cluster was enclosed inside a larger one, with tetrahedral bonding between them.[50] Other theoretical works, however, have suggested that similarly sized bulklike particles are more stable.[51] The optical properties of hollow and core−shell structures have also been studied by Hamad et al.[52] They predicted the band gap of the hollow clusters to oscillate between 4.4 and 4.7 eV. The gap of core−shell clusters was found to be smaller. Similar sized bulklike clusters exhibit a narrower band gap in the range 3.6−4.0 eV.

Further computational works concerning larger ZnS clusters up to $n \sim 500$ predicted the BCT crystalline structure to be the most stable.[50] It has been proposed that BCT is able to accommodate distortions more easily than bulklike structures. Indeed, wurtzite and sphalerite polymorphs undergo significant rearrangements in order to minimize both the number of dangling bonds in the surface and the net dipole of the structure. Nevertheless, the BCT phase has not been reported experimentally. Moreover, the wurtzite phase was predicted to be only slightly higher in energy than the BCT phase and was expected to be further stabilized in solution. Sphalerite was found to be the least stable out of the three investigated phases. Even if a significant effort has been devoted to the structural elucidation of ZnS nanoparticles with sizes comparable to the experiments, the studies regarding their electronic and optical properties are rather scarce.

The comparison of the optical properties of small ZnO and ZnS clusters with the experimental results is quite difficult since the absorption and luminescence onset shifts with the particle size due to the aforementioned quantum size effect. Thus, the choice of an appropriate model is mandatory. The three-dimensional $(ZnO)_{111}$ cluster saturated by water molecules proposed by some of us[53] has shown to accurately reproduce the experimental optical features of ZnO nanoparticles in the framework of the time-dependent DFT (TDDFT). In the present theoretical work we further progress with the modeling of ZnO and ZnS nanostructures by defining new realistic nanoparticle models for each material and investigating their structural, electronic, and optical properties by means of DFT/TDDFT calculations employing GGA and hybrid functionals. To the best of our knowledge, this is the first time that the optical properties of a realistically large ZnS nanoparticle model are investigated.

2. MODEL AND COMPUTATIONAL DETAILS

To provide a direct comparison of calculated data to experimentally characterized nanoparticles, realistic 3D $(ZnX)_{111}$ nanoclusters have been set up starting from the bulk wurtzite. Such ∼1.5 nm sized nanoparticles are prismatic in shape, as shown in Figure 1. The stability of similar prismatic nanocrystals has been reported for ZnO[41] and ZnS.[54] The dangling bonds in the surface of such bulklike structures lead to artificial surface states that intrude into the band gap. In the particular case of the noncentrosymmetric wurtzite structure, the polarity of the Zn- and X- (X = O, S hereafter) terminated (0001) and (000$\bar{1}$) surfaces establishes an unrealistic net dipole moment along the c axis, which diverges with increasing dimension along this axis, as well as the surface energy.[37,41,55] Due to these reasons, the band gap narrows and the nanostructures become metallic, leading to methodological and conceptual troubles. Surface reconstruction and/or proper saturation of unsaturated sites has shown to remove the surface states and decrease the dipole along the c axis, opening the band gap and stabilizing the nanoparticle. Therefore, and in a first step, we saturate the polar surfaces by dissociating H_2X molecules, adsorbing H^+ and HX^- ions on the unsaturated X and Zn sites respectively. The dissociative adsorption of water in the polar surfaces of ZnO has been found to be

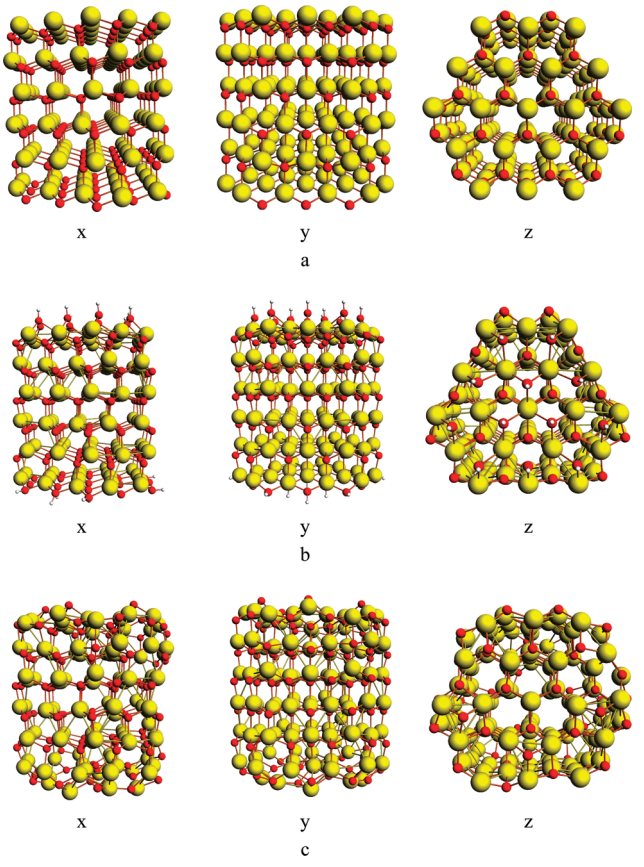

Figure 1. Geometrical structures of (a) unrelaxed $(ZnO)_{111}$ cut from the bulk, (b) relaxed $[(ZnO)_{111}(H_2O)_{12}]$, and (c) relaxed $[(ZnO)_{111}(ZnO)_5]$. Similar structures have been obtained for ZnS.

energetically favorable;[37] thus, we follow the same approach for ZnS. In a second step, we place Zn^{2+} and X^{2-} instead of H^+ and HX^- ions, respectively, to recover stoichiometric clusters composed exclusively of Zn and X.

The investigated models have been fully optimized by means of Car−Parrinello molecular dynamics,[56] as implemented in the Quantum-Espresso package,[57] employing the GGA-PBE exchange-correlation functional[58] in combination with a plane wave basis set and ultrasoft pseudopotentials.[59,60] Plane wave basis set cutoffs set for the smooth part of the wave functions and the augmented density are 25 and 200 Ry, respectively. The dimensions of the simulation supercells have been defined by adding 7 Å of vacuo to the largest nanoparticle dimension in each direction. Geometry optimization has been carried out by performing a preliminary dynamic simulation at finite temperature, with an integration time step of 5 au, to explore the potential energy surface of the system. Then we introduce a friction of 0.005 for the electronic degrees of freedom to reach the structural minimum. The fictitious mass used for the electronic degrees of freedom is 500 au, and we set the masses for both S and Zn atoms to 5.0 amu. This setup allows us to perform a rapid nuclear thermalization and to maintain the adiabaticity throughout the simulation. Suitable structures sampled during the dynamics have been further optimized using the PBE functional together with a double-valence set of Slater-type orbitals as implemented in the ADF program package.[61]

While satisfactorily reproducing structural parameters, GGA functionals severely underestimate the band gap of II−VI semiconductor materials. Thus, the hybrid B3LYP functional has been employed in conjunction with an SVP basis set to perform TDDFT calculations on the optimized structures. The B3LYP functional has been modified to contain 27.5% Hartree−Fock exchange, as from our previous work.[53] Solvation effects have been included by means of the polarizable continuum model (PCM). We chose water as solvent to reproduce the experimental conditions since an increasing number of II−VI nanostructures are synthesized in water solution. This setup has shown to accurately reproduce the absorption properties of ZnO nanostructures.[53] All TDDFT calculations have been performed by the Gaussian03 program package.[62]

3. RESULTS AND DISCUSSION

3.1. Geometry. As shown in Figure 1, all the atoms in the apolar surfaces (see views along x and y axes in Figure 1) of the unrelaxed $(ZnX)_{111}$ structures are threefold coordinated while each polar surface (see view along z axis in Figure 1) bears in our models nine twofold coordinated ions. Thus, following previous works,[37,38,53] the saturation of the polar surfaces with a variable number of H_2X molecules was studied. Binding of 11 or 12 dissociated H_2X molecules to the polar surfaces of the nanostructures ($[(ZnX)_{111}(H_2X)_{12}]$ model hereafter) led to the saturation of two-coordinated surface atoms and at the same time to the minimization of the dipole along the *c* axis. In a second step, we substituted H^+ and HX^- with surface Zn^{2+} and X^{2-} ions on the X- and Zn-terminated surfaces, respectively. Proper charge compensation was achieved, by addition of five Zn^{2+} and five X^{2-} ions to the X- and Zn-terminated faces, leading to the $[(ZnX)_{111}(ZnX)_5]$ model. We need to mention here that while for H^+/HX^- saturation a rather straightforward geometry optimization was achieved, for the models saturated with Zn^{2+}/X^{2-} ions we had to perform several Car−Parrinello molecular dynamics simulations, carrying the system at 500 K for 2−3 ps followed by annealing at 0 temperature, to locate a reasonable minimum energy structure.

Bulklike clusters undergo a significant structural rearrangement upon optimization. Such reconstruction has been attributed to the unsaturated atoms on the surface. Since we have saturated the dangling bonds, our models preserve the wurtzite structure (Figure 1). It is worth noting that the surface atoms in the relaxed structures remain at least threefold coordinated. However, there is a noticeable deviation from the ideal bulklike structure.

In order to reveal the distortion of the optimized nanoparticles, the average Zn−X bond length of each atom with its neighbors has been calculated. Figure 2 shows the variation of such bond lengths as a function of the position of the atom with respect to the center of the cluster. The bonds in the center of the nanoparticle are slightly longer than those experimentally observed in the bulk. The Zn−O bonds in the core of the nanoparticle are 2.05 Å on average, 5% larger compared to the experimental value of 1.95 Å reported for the bulk material. In the case of ZnS, our calculations provide Zn−S bonds of ∼2.42 Å in the center of the nanoparticle, 3% longer than the value of 2.35 Å observed in the bulk. With the increasing distance with respect to the center of the nanoparticle, the pattern of the bond lengths turns out to be more complicated. Even if some bonds remain as large as those measured in the inner part, most of them show a significant contraction with respect to the core and tend to converge to the value observed in the bulk, irrespective of ZnO or ZnS and of the model. These findings reveal a surface

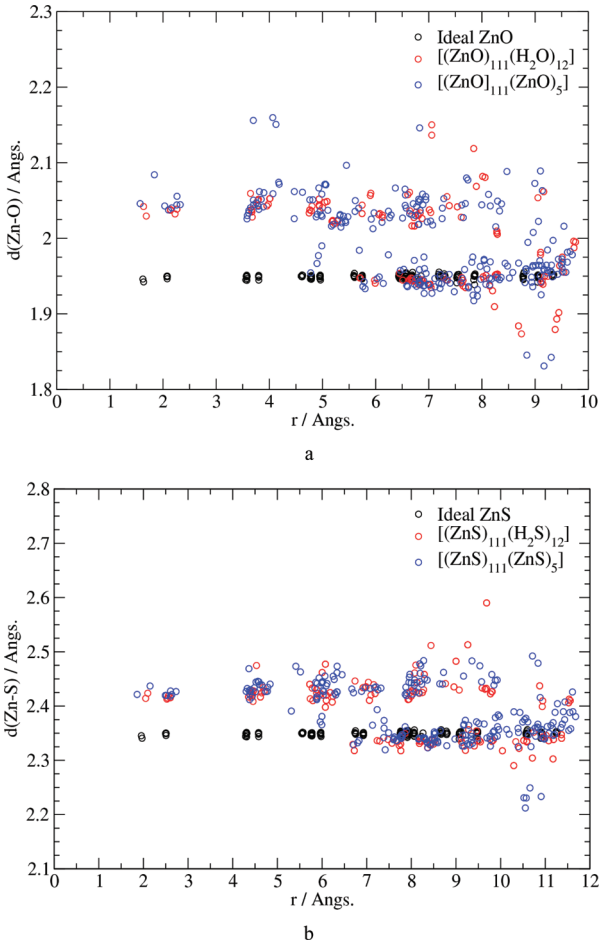

Figure 2. Zn−X bond length of each atom with its neighbors as a function of the position of the atom with respect to the center of the cluster. For sake of clarity, surface-attached H_2X molecules have not been taken into account in the case of $[(ZnX)_{111}(H_2X)_{12}]$ models. (a) ZnO and (b) ZnS.

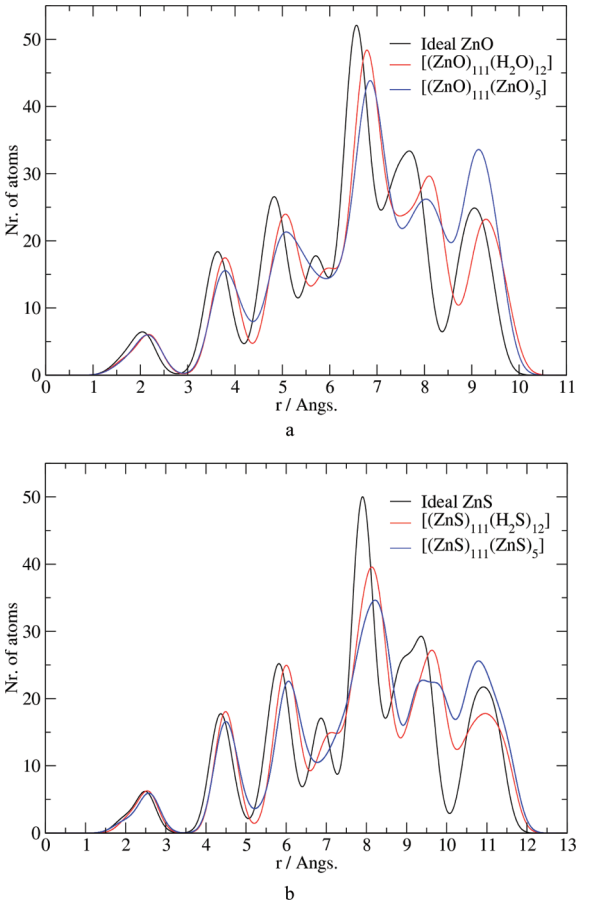

Figure 3. Radial distribution function. For sake of clarity, surface-attached H_2X molecules have not been taken into account in the case of $[(ZnX)_{111}(H_2X)_{12}]$ models. (a) ZnO and (b) ZnS.

reconstruction that bring some of the surface ions closer, even in the presence of passivating ligands. The lower coordination of the surface seems to be the driving force of the shrinkage of the bonds in the outer region.

In order to better characterize the structural reconstruction, the radial distribution function (RDF hereafter) of the relaxed nanoparticles has been calculated. The RDF indicates the number of atoms located at a given distance with respect to a particular point. Figure 3 displays the RDFs of the optimized models together with that of the unrelaxed wurtzite structure, taking the center of the cluster as the origin. The core of the optimized nanoparticles resembles the ideal wurtzite structure, with three well-defined shells of atoms. Nevertheless, such inner atoms are slightly shifted outward if compared with the ideal structure, and therefore the bonds are correspondingly longer. Beyond a given radius (∼5.5 and ∼6.5 Å from the nanoparticle center for ZnO and ZnS, respectively) the RDF of the optimized nanoparticles substantially deviates from ideal structure, meaning a significant structural reconstruction. The study of the RDF of Zn and X atoms separately (see the Supporting Information) reveals that in the outermost region of the nanoparticle the X atoms are displaced outward with respect to the Zn atoms. A similar reconstruction has already been reported not only for ZnS[51] but also for CdS and CdSe.[63−65] Indeed metal atoms prefer a higher coordination, while X atoms, be it oxygen or sulfur, can accommodate a lower coordination environment.

Given the importance of the polar surfaces on the stability of the investigated materials, we performed a closer inspection of the reconstruction of the Zn- and X- terminated surfaces, and we calculated the average bond length of each atom in the polar surfaces with its neighbors. The results, reported in the Supporting Information, show that the optimized $[(ZnX)_{111}(H_2X)_{12}]$ structures exhibit a more regular geometry than $[(ZnX)_{111}(ZnX)_5]$ structures. While in the ideal wurtzite there are eight clusters of atoms that are symmetrically placed with respect to the center of the plane, for the $[(ZnX)_{111}(ZnX)_5]$ models a more disordered pattern of bond lengths is found, revealing that the atoms are not regularly placed with respect to the center of the polar planes. We thus conclude that $[(ZnX)_{111}(ZnX)_5]$ models show a larger reconstruction of the polar surfaces. Indeed, as mentioned before, $[(ZnX)_{111}(H_2X)_{12}]$ nanoparticles were rather straightforwardly optimized, while several Car−Parrinello molecular dynamics simulations had to be carried out to converge the $[(ZnX)_{111}(ZnX)_5]$ nanostructures.

3.2. Electronic Structure and Absorption Spectra. The investigated ZnO and ZnS model systems exhibit a well-opened HOMO−LUMO energy gap, meaning that the saturation of the polar faces and the surface reconstruction effectively removes the presence of possible artificial intraband-gap states. For sake of

dx.doi.org/10.1021/jp2083709 |J. Phys. Chem. C 2011, 115, 25219–25226

Table 1. Energies of the Frontier Orbitals and Band Gaps, in eV

	$[(ZnO)_{111}(H_2O)_{12}]$	$[(ZnO)_{111}(ZnO)_5]$	$[(ZnS)_{111}(H_2S)_{12}]$	$[(ZnS)_{111}(ZnS)_5]$
HOMO−1	−6.33	−6.64	−7.09	−6.81
HOMO	−6.30	−6.56	−7.07	−6.73
LUMO	−2.25	−2.32	−2.29	−2.22
LUMO+1	−1.63	−1.89	−1.88	−1.88
LUMO+2	−1.62	−1.78	−1.70	−1.75
HOMO−LUMO	4.05	4.24	4.77	4.51

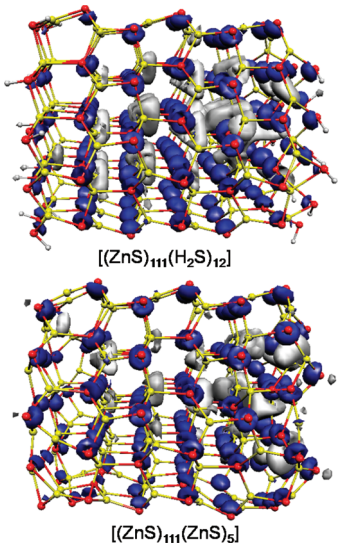

Figure 4. Isodensity plots of the LUMO for $[(ZnS)_{111}(H_2S)_{12}]$ (top) and $[(ZnS)_{111}(ZnS)_5]$ (bottom).

comparison the band-gap values of the nanoparticles are shown in Table 1, together with the DFT eigenvalues of the frontier Kohn−Sham single-particle molecular orbitals. It is worth noting that ZnS exhibits a wider gap than ZnO (4.77 vs 4.05 eV for the $[(ZnX)_{111}(H_2X)_{12}]$ model and 4.51 vs 4.24 eV for the $[(ZnX)_{111}(ZnX)_5]$ model). As from our previous results on $[(ZnO)_{111}(H_2O)_{12}]$,[53] for all the investigated systems the LUMO is a delocalized conduction band state, which, despite having the same nature of the higher lying orbitals, is quite separated in energy from the rest of the conduction band states; see Table 1 and Figure 4. The presence of this state is independent from the specific material or saturation pattern (see Figure 4 for the isodensity plot of the LUMO for $[(ZnS)_{111}(H_2S)_{12}]$ and $[(ZnS)_{111}(ZnS)_5]$) and might therefore be an intrinsic property of the considered nanostructures.

Inspection of the energies of the HOMO and the LUMO reveals that the energy of the latter remains relatively similar for ZnO and ZnS, irrespective of the model. Therefore, the wider band gap of ZnS is calculated here to be a consequence of the lower HOMO energy. From these results we thus conclude that both models can be safely employed to determine the systems optical properties, despite $[(ZnO)_{111}(H_2O)_{12}]$ showing a slightly narrower band gap than $[(ZnO)_{111}(ZnO)_5]$, whereas $[(ZnS)_{111}(H_2S)_{12}]$ exhibits a slightly wider gap than $[(ZnS)_{111}(ZnS)_5]$.

Even if the differences of the Kohn−Sham molecular orbital eigenvalues may provide a reasonable approximation to the band-gap transition energies of bulk ZnO and ZnS, the precise description of the excitation energies in confined nanostructures requires a more accurate picture of electron correlation, such as that provided by TDDFT, which takes into account not only the electron−hole interaction and exchange-correlation effects, but also the configurational mixing of single excitations. The TDDFT-calculated electronic transition energies corresponding to the lowest excited states of the nanoparticles studied are given in Table 2 along with the calculated oscillator strengths. The energies of the low-lying excited states are in excellent agreement with the experimental absorption onsets reported for ∼1.5 nm sized ZnO and ZnS nanoparticles (3.70 eV[25] and 4.40 eV,[27] respectively). For ZnO and ZnS we calculate lowest excitation energies at, respectively, 3.6 and 3.7 eV and 4.3 and 4.1 eV, for $[(ZnX)_{111}(H_2X)_{12}]$ and $[(ZnX)_{111}(ZnX)_5]$ models, respectively. From the comparison of $[(ZnX)_{111}(H_2X)_{12}]$ and $[(ZnX)_{111}(ZnX)_5]$ models, we notice, as previously mentioned, that the type of saturation of the polar surfaces does not seem to play a significant role in the excitation energies, with maximum deviations within 0.2 eV. However, the low-lying excitation energies of $[(ZnO)_{111}(H_2O)_{12}]$ are slightly red-shifted with respect to $[(ZnO)_{111}(ZnO)_5]$, while for ZnS the trend is the opposite. This could be predicted from the band-gap values.

In order to get a better understanding of the electronic structure of the investigated nanoparticles, their density of states (DOS hereafter) has been plotted (Figure 5 and Figure 6) and their valence band structure has been studied. Since all the binary tetrahedrally coordinated semiconductors exhibit a similar valence band structure, the identification of the observed peaks can be rather straightforward. Following the notation proposed in the literature[66] we have labeled the main valence band features as P_I, P_{II}, d, and P_{III}. P_I arises from the valence p orbitals of the X atoms. P_{II} and d are related to the 4s and 3d orbitals of the Zn atoms, respectively. P_{III} has been attributed to the valence s orbitals of X.

The d peak of binary semiconductors has been exhaustively studied by photoelectron spectroscopy and X-ray absorption spectroscopy. In the investigated nanoparticles, the position of the d band with respect to the top of the valence band (valence band maximum, VBM hereafter) is in good agreement with the experimentally reported binding energy differences, which are measured to lie in the range 7.5−10.0 eV for bulk ZnO[66−69] and ∼9.0 eV for bulk ZnS.[66] Our calculated binding energies are only slightly displaced to lower values. In fact, and depending on the model, our calculations provide binding energies of 7.3−7.5 eV for ZnO and 8.6−8.8 eV for ZnS. A similar underestimate has been observed in recent high-level DFT and GW calculations regarding bulk ZnO[70] and ZnS.[71,72] Calculated binding energies were reported in the range 6.1−6.9 and 7.1−7.5 eV for ZnO and ZnS, respectively. If the Zn 3d orbitals are assumed to be relatively stable with the size of the nanostructure, when moving from the bulk to the nanoscale the VBM supposedly shifts to lower energies due to the quantum confinement effect.

Table 2. Lowest TDDFT Excitation Energies, in eV; Oscillator Strengths in Parentheses[a]

	$[(ZnO)_{111}(H_2O)_{12}]$	$[(ZnO)_{111}(ZnO)_5]$	$[(ZnS)_{111}(H_2S)_{12}]$	$[(ZnS)_{111}(ZnS)_5]$
1	3.59 (0.0017)	3.69 (0.0426)	4.26 (0.0019)	4.05 (0.1018)
2	3.62 (0.0119)	3.74 (0.0473)	4.34 (0.0651)	4.09 (0.0450)

[a] Experimental values for ZnO and ZnS are 3.70 and 4.40 eV, respectively, from refs 25 and 27.

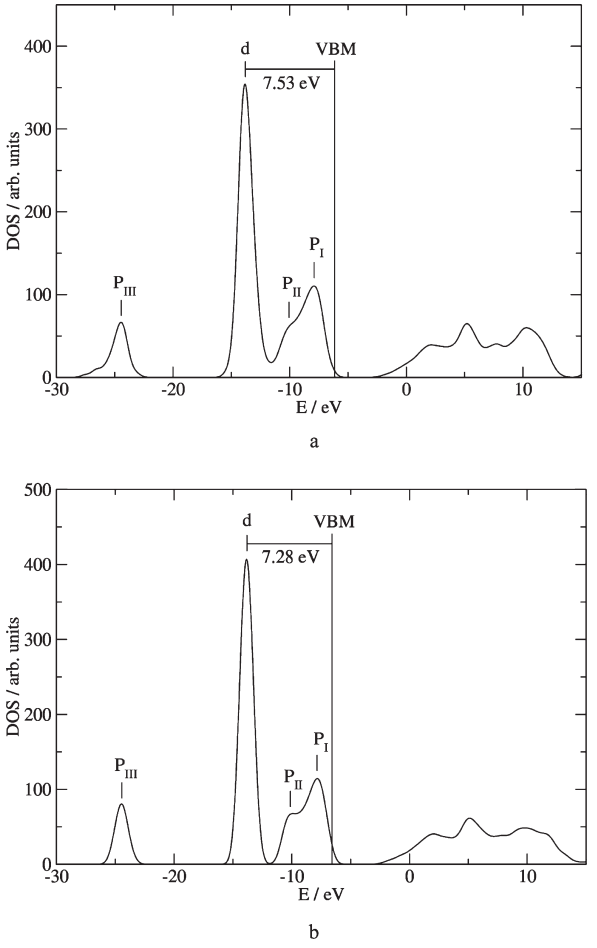

Figure 5. Density of states of (a) $[(ZnO)_{111}(H_2O)_{12}]$ and (b) $[(ZnO)_{111}(ZnO)_5]$.

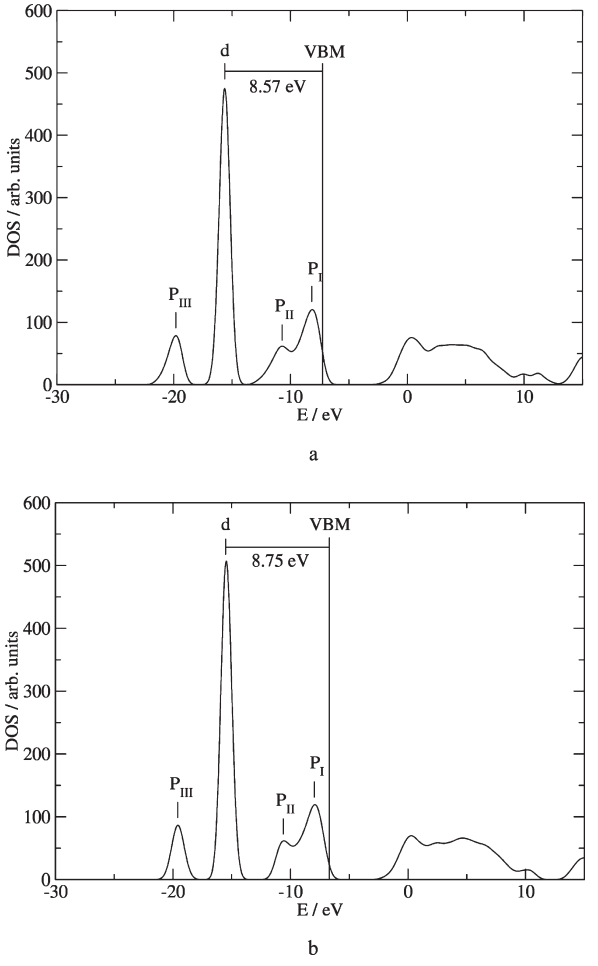

Figure 6. Density of states of (a) $[(ZnS)_{111}(H_2S)_{12}]$ and (b) $[(ZnS)_{111}(ZnS)_5]$.

Therefore, we speculate that the binding energies are shifted to lower values, in line with our results. In a similar fashion, the binding energies calculated for the other peaks are to some extent underestimated with respect to the corresponding experimental quantities measured for bulk ZnO and ZnS, even though the agreement is quite good, Supporting Information. It is worth noting that $[(ZnX)_{111}(H_2X)_{12}]$ and $[(ZnX)_{111}(ZnX)_5]$ models roughly provide the same picture of the valence band structure of both ZnO and ZnS. P_I and P_{II} are slightly closer for ZnO than for ZnS. Indeed, P_{II} is only 2.0−2.2 eV deeper than P_I in the valence band of ZnO, whereas for ZnS the gap is around 2.6 eV. These findings suggest a greater mixing of 2p orbitals of O and 4s orbitals of Zn in ZnO. Furthermore, the d peak is closer to P_{II} in ZnO. In fact, the energy difference between the d peak and P_{II} lies in the range 3.8−3.9 eV for ZnO, the gap being around 4.9 eV in the case of ZnS. Finally P_{III} and d peak are significantly closer for ZnS than for ZnO, the gaps being 4.1 and 10.6 eV, respectively. This observation means a greater hybridization of 3d orbitals of Zn and 3s orbitals of S in ZnS.

4. CONCLUSIONS

We have reported on the modeling of ZnO and ZnS nanostructures by defining novel nanoparticle models for each material and investigating their structural, electronic, and optical properties by means of DFT/TDDFT calculations employing a GGA and hybrid functionals. To set up a proper comparison of the optical properties of small ZnO and ZnS clusters with the experimental results, the choice of an appropriate model is mandatory since the absorption and luminescence onsets shift with the particle size due to the quantum size effect. To provide a direct comparison of calculated data to experimentally characterized nanoparticles, realistic 3D $(ZnX)_{111}$ nanoclusters ∼1.5 nm sized of prismatic shape have been set up starting from the bulk wurtzite

(X = O, S). Our modeling strategy followed two lines: (i) we saturated the polar surfaces of ZnX nanoparticles by dissociating H_2X molecules, adsorbing H^+ and HX^- ions on the unsaturated X and Zn sites, respectively; and (ii) we added Zn^{2+} and X^{2-} instead of H^+ and HX^- ions, respectively, to the polar surfaces to recover stoichiometric clusters composed exclusively of Zn and X.

The investigated models were fully optimized by means of Car−Parrinello molecular dynamics and local geometry optimization techniques. While for H^+/HX^- saturation a rather straightforward geometry optimization was achieved, for the models saturated with Zn^{2+}/X^{2-} ions we had to perform several Car−Parrinello molecular dynamics simulations at finite temperature, followed by annealing at zero temperature, to locate a reasonable minimum energy structure. Bulklike clusters were found to undergo a significant structural rearrangement upon optimization but preserved the wurtzite structure. Such reconstruction has been attributed to the unsaturated atoms on the surface.

The investigated ZnO and ZnS model systems exhibit a well-opened HOMO−LUMO energy gap, meaning that the saturation of the polar faces and the surface reconstruction effectively remove the presence of possible artificial intraband-gap states. TDDFT calculation of the lowest excitation energies for all studied systems in water solution were in excellent agreement with the experimental absorption onsets reported for ∼1.5 nm sized ZnO and ZnS nanoparticles (3.70 and 4.40 eV, respectively). For $[(ZnX)_{111}(H_2X)_{12}]$ and $[(ZnX)_{111}(ZnX)_5]$ we calculate lowest excitation energies at, respectively, 3.6 and 4.3 eV and 3.7 and 4.1 eV for X = O and S, respectively. From the comparison of $[(ZnX)_{111}(H_2X)_{12}]$ and $[(ZnX)_{111}(ZnX)_5]$ models we therefore concluded that the type of saturation of the polar surfaces does not seem to play a significant role in determining the excitation energies.

We then investigated the electronic structure of the considered nanoparticles, with reference to the valence band structure, in terms of their density of states. The position of the d band with respect to the top of the valence band maximum was in good agreement with the experimentally reported binding energy differences, which are measured in the range 7.5−10.0 and 9.0 eV for bulk ZnO and ZnS, respectively. Our calculated binding energies are only slightly displaced toward lower values. Our calculations provide binding energies of 7.3−7.5 eV for ZnO and 8.6−8.8 eV for ZnS. The 3d orbitals belong to the semicore of the Zn atom, and their position is expected to be relatively stable irrespective of the size of the nanostructure. On the other hand, when moving from the bulk to the nanoscale the valence band maximum supposedly shifts to lower energies due to the quantum confinement effect so that the binding energies are expected to shift to lower values, in line with our results.

In conclusion, we have reported a comprehensive computational modeling investigation of ZnO and ZnS nanostructures, defining realistic models and a highly accurate computational strategy. We believe this work to provide the required computational framework for the investigation of ligand binding to ZnX nanostructures, thus aiding the understanding of the subtle interactions between the ligands and the semiconductor in defining the peculiar optical properties of these systems.

■ ASSOCIATED CONTENT

Supporting Information. Radial distribution functions and bond pattern analyses; binding energies; references. This material is available free of charge via the Internet at http://pubs.acs.org.

■ AUTHOR INFORMATION

Corresponding Author
*E-mail filippo@thch.unipg.it.

■ ACKNOWLEDGMENT

We acknowledge FP7-ENERGY-2010 project 261920 "ESCORT", CNR-EFOR and Istituto Italiano di Tecnologia, Project Seed 2009 "HELYOS", for financial support. J.M.A. thanks the Spanish Ministry of Education for funding through a FPU Fellowship.

■ REFERENCES

(1) Alivisatos, A. P. *J. Phys. Chem.* **1996**, *100*, 13226–13239.
(2) Hoffman, A. J.; Mills, G.; Yee, H.; Hoffmann, M. R. *J. Phys. Chem.* **1992**, *96*, 5546–5552.
(3) Kuwabata, S.; Nishida, K.; Tsuda, R.; Inoue, H.; Yoneyama, H. *J. Electrochem. Soc.* **1994**, *141*, 1498–1503.
(4) Chakrabarti, R.; Dutta, J.; Bandyopadhyay, S.; Bhattacharyya, D.; Chaudhuri, S.; Pal, A. K. *Sol. Energy Mater. Sol. Cells* **2000**, *61*, 113–126.
(5) Chu, T. L.; Chu, S. S. *Solid-State Electron.* **1995**, *38*, 533–549.
(6) Contreras, G.; Vigil, O.; Ortega, M.; Morales, A.; Vidal, J.; Albor, M. L. *Thin Solid Films* **2000**, *361−362*, 378–382.
(7) Edwards, P. R.; Gallogay, S. A.; Durose, K. *Thin Solid Films* **2000**, *361−362*, 364–370.
(8) Corcoran, E. *Sci. Am.* **1990**, *263*, 74.
(9) Sebastian, P. J.; Ocampo, M. *Sol. Energy Mater. Sol. Cells* **1996**, *44*, 1–10.
(10) Medintz, I. L.; Uyeda, H. T.; Goldman, E. R.; Mattoussi, H. *Nat. Mater.* **2005**, *4*, 435–446.
(11) Fang, X.; Bando, Y.; Gautam, U. K.; Zhai, T.; Zeng, H.; Xu, X.; Liao, M.; Golberg, D. *Crit. Rev. Solid State Mater. Sci.* **2009**, *34*, 190–223.
(12) Li, S.; Yang, G. W. *J. Phys. Chem. C* **2010**, *114*, 15054–15060.
(13) Wang, Z.; Daemen, L. L.; Zhao, Y.; Zha, C. S.; Downs, R. T.; Wang, X.; Wang, Z. L.; Hemley, R. J. *Nat. Mater.* **2005**, *4*, 922–927.
(14) Zhang, H.; Huang, F.; Gilbert, B.; Banfield, J. F. *J. Phys. Chem. B* **2003**, *107*, 13051–13060.
(15) Huang, F.; Banfield, J. F. *J. Am. Chem. Soc.* **2005**, *127*, 4523–4529.
(16) Liu, W. *Mater. Lett.* **2006**, *60*, 551–554.
(17) Murakoshi, K.; Hosokawa, H.; Yanagida, S. *Jpn. J. Appl. Phys.* **1999**, *38*, 522–527.
(18) Sun, J. Q.; Shen, X. P.; Chen, K. M.; Liu, Q.; Liu, W. *Solid State Commun.* **2008**, *147*, 501–504.
(19) Tong, H.; Zhu, Y. J.; Yang, L. X.; Li, L.; Zhang, L.; Chang, J.; An, L. Q.; Wang, S. W. *J. Phys. Chem. C* **2007**, *111*, 3893–3900.
(20) Zhao, Y.; Zhang, Y.; Zhu, H.; Hadjipanayis, G. C.; Xiao, J. Q. *J. Am. Chem. Soc.* **2004**, *126*, 6874–6875.
(21) Qadri, S. B.; Skelton, E. F.; Dinsmore, A. D.; Hu, J. Z.; Kim, W. J.; Nelson, C.; Ratna, B. R. *J. Appl. Phys.* **2001**, *89*, 115–119.
(22) Zhang, H.; Gilbert, B.; Huang, F.; Banfield, J. F. *Nature* **2003**, *424*, 1025–1029.
(23) Kahn, M. L.; Cardinal, T.; Bousquet, B.; Monge, M.; Jubera, V.; Chaudret, B. *ChemPhysChem* **2006**, *7*, 2392–2397.
(24) Monticone, S.; Tufeu, R.; Kanaev, A. V. *J. Phys. Chem. B* **1998**, *102*, 2854–2862.
(25) van Dijken, A.; Meulenkamp, E. A.; Vanmaekelbergh, D.; Meijerink, A. *J. Phys. Chem. B* **2000**, *104*, 1715–1723.
(26) Djurisic, A. B.; Leung, Y. H. *Small* **2006**, *2*, 944–961.
(27) Biswas, S.; Kar, S. *Nanotechnology* **2008**, *19*, 045710(1–11).
(28) Souici, A. H.; Keghouche, N.; Delaire, J. A.; Remita, H.; Mostafavi, M. *Chem. Phys. Lett.* **2006**, *422*, 25–29.
(29) Liu, C.; Chung, S. Y.; Lee, S.; Weiss, S.; Neuhauser, D. *J. Chem. Phys.* **2009**, *131*, 174705(1–8).
(30) Kar, S.; Biswas, S.; Chaudhuri, S. *Nanotechnology* **2005**, *16*, 737–740.
(31) Kar, S.; Chaudhuri, S. *J. Phys. Chem. B* **2005**, *109*, 3298–3302.

(32) Kar, S.; Chaudhuri, S. *Chem. Phys. Lett.* **2005**, *414*, 40–46.
(33) Tang, H.; Xu, G.; Weng, L.; Pan, L.; Wang, L. *Acta Mater.* **2004**, *52*, 1489–1494.
(34) Janotti, A.; de Walle, C. G. V. *Phys. Rev. B* **2007**, *76*, 165202(1–22).
(35) Kohan, A. F.; Ceder, G.; Morgan, D. *Phys. Rev. B* **2000**, *61*, 15019–15027.
(36) Lany, S.; Zunger, A. *Phys. Rev. B* **2005**, *72*, 035215(1–13).
(37) Meyer, B. *Phys. Rev. B* **2004**, *69*, 045416(1–10).
(38) Meyer, B.; Marx, D.; Dulub, O.; Diebold, U.; Kunat, M.; Langenberg, D.; Wöll, D. *Angew. Chem., Int. Ed.* **2004**, *43*, 6641–6645.
(39) Muscat, J.; Wander, A.; Harrison, N. M. *Chem. Phys. Lett.* **2001**, *342*, 397–401.
(40) Patterson, C. H. *Phys. Rev. B* **2006**, *74*, 144432(1–13).
(41) Li, C.; Guo, W.; Kong, Y.; Gao, H. *Appl. Phys. Lett.* **2007**, *90*, 223102(1–3).
(42) Matxain, J. M.; Mercero, J. M.; Fowler, J. E.; Ugalde, J. M. *J. Am. Chem. Soc.* **2003**, *125*, 9494–9499.
(43) Schrier, J.; Demchenko, D. O.; Wang, L. W.; Alivisatos, A. P. *Nano Lett.* **2007**, *7*, 2377–2382.
(44) Shen, X.; Allen, P. B.; Muckerman, J. T.; Daveport, J. W.; Zheng, J. C. *Nano Lett.* **2007**, *7*, 2267–2271.
(45) Wang, B.; Nagase, S.; Zhao, J.; Wang, G. *J. Phys. Chem. C* **2007**, *111*, 4956–4963.
(46) Matxain, J. M.; Fowler, J. E.; Ugalde, J. M. *Phys. Rev. A* **2000**, *61*, 053201(1–8).
(47) Matxain, J. M.; Irigoras, A.; Fowler, J. E.; Ugalde, J. M. *Phys. Rev. A* **2001**, *64*, 013201(1–7).
(48) Spanó, E.; Hamad, S.; Catlow, C. R. A. *J. Phys. Chem. B* **2003**, *107*, 10337–10340.
(49) Spanó, E.; Hamad, S.; Catlow, C. R. A. *Chem. Commun.* **2004**, *7*, 864–865.
(50) Hamad, S.; Catlow, R. A. *J. Cryst. Growth* **2006**, *294*, 2–8.
(51) Pal, S.; Goswami, B.; Sarkar, P. *J. Chem. Phys.* **2005**, *123*, 044311(1–9).
(52) Hamad, S.; Catlow, C. R. A.; Spanó, E.; Matxain, J. M.; Ugalde, J. M. *J. Phys. Chem. B* **2005**, *109*, 2703–2709.
(53) De Angelis, F.; Armelao, L. *Phys. Chem. Chem. Phys.* **2011**, *13*, 467–475.
(54) Hamad, S.; Cristol, S.; Catlow, C. R. A. *J. Phys. Chem. B* **2002**, *106*, 11002–11008.
(55) Wander, A.; Harrison, N. M. *J. Chem. Phys.* **2001**, *115*, 2312–2316.
(56) Car, R.; Parrinello, M. *Phys. Rev. Lett.* **1985**, *55*, 2471–2474.
(57) Giannozzi, P.; Baroni, S.; Bonini, N.; Calandra, M.; Car, R.; Cavazzoni, C.; Ceresoli, D.; Chiarotti, G. L.; Cococcioni, M.; Dabo, I. et al. *J. Phys.: Condens. Matter* **2009**, *21*, 395502(1–19).
(58) Perdew, J. P.; Burke, K.; Ernzerhof, M. *Phys. Rev. Lett.* **1996**, *77*, 3865–3868.
(59) Giannozzi, P.; De Angelis, F.; Car, R. *J. Chem. Phys.* **2004**, *120*, 5903–5915.
(60) Pasquarello, A.; Car, K. L. R.; Lee, C.; Vanderbilt, D. *Phys. Rev. Lett.* **1992**, *69*, 1982–1985.
(61) te Velde, G.; Bickelhaupt, F. M.; Baerends, E. J.; Fonseca Guerra, C.; van Gisbergen, S. J. A.; Snijders, J. G.; Ziegler, T. *J. Comput. Chem.* **2001**, *22*, 931–967.
(62) Frisch, M. J.; Trucks, G. W.; Schlegel, H. B.; Scuseria, G. E.; Robb, M. A.; Cheeseman, J. R.; Montgomery, J. A.; Vreven, T.; Kudin, K. N.; Burant, J. C.; et al. *Gaussian 03*, revision D.01; Gaussian, Inc.: Pttsburgh, PA, 2004.
(63) Joswig, J.-O.; Springborg, M.; Seifert, G. *J. Phys. Chem. B* **2000**, *104*, 2617–2622.
(64) Leung, K.; Pokrant, S.; Whaley, K. B. *Phys. Rev. B* **1998**, *57*, 12291–12301.
(65) Sarkar, P.; Springborg, M. *Phys. Rev. B* **2003**, *68*, 235409(1–7).
(66) Ley, L.; Pollak, R. A.; McFeely, F. R.; Kowalczyk, S. P.; Shirley, D. A. *Phys. Rev. B* **1974**, *9*, 600–621.
(67) Powell, R. A.; Spicer, E.; McMenamin, J. C. *Phys. Rev. B* **1972**, *6*, 3056–3065.
(68) Vesely, C. J.; Hengehold, R. L.; Langer, D. W. *Phys. Rev. B* **1972**, *5*, 2296–2301.
(69) Zwicker, G.; Jacobi, K. *Solid State Commun.* **1985**, *54*, 701–704.
(70) Labat, F.; Ciofini, I.; Adamo, C. *J. Chem. Phys.* **2009**, *131*, 044708(1–11).
(71) Rinke, P.; Qteish, A.; Neugebauer, J.; Freysoldt, C.; Scheffler, M. *New J. Phys.* **2005**, *7*, 126(1–35).
(72) Shishkin, M.; Kresse, G. *Phys. Rev. B* **2007**, *75*, 235102(1–9).